Graphene Oxide Induces Toll-like Receptor 4 (TLR4)-Dependent Necrosis in Macrophages

Guangbo Qu,[†] Sijin Liu,[†,*] Shuping Zhang,[†] Lei Wang,[†] Xiaoyan Wang,[†] Bingbing Sun,[‡] Nuoya Yin,[†] Xiang Gao,[§] Tian Xia,[‡] Jane-Jane Chen,[⊥] and Gui-Bin Jiang[†]

[†]State Key Laboratory of Environmental Chemistry and Ecotoxicology, Research Center for Eco-Environmental Sciences, Chinese Academy of Sciences, Beijing 100085, China, [‡]Division of NanoMedicine, Department of Medicine, University of California, Los Angeles, California 90095, United States, [§]Model Animal Research Center, Nanjing University, Jiangsu 210032, China, and [⊥]Institute for Medical Engineering and Science, Massachusetts Institute of Technology, Cambridge, Massachusetts 02139, United States

ABSTRACT Graphene and graphene-based nanomaterials display novel and beneficial chemical, electrical, mechanical, and optical characteristics, which endow these nanomaterials with promising applications in a wide spectrum of areas such as electronics and biomedicine. However, its toxicity on health remains unknown and is of great concern. In the present study, we demonstrated that graphene oxide (GO) induced necrotic cell death to macrophages. This toxicity is mediated by activation of toll-like receptor 4 (TLR4) signaling and subsequently in part *via* autocrine TNF-α production. Inhibition of TLR4 signaling with a selective inhibitor prevented cell death nearly completely. Furthermore, *TLR4*-deficient bone marrow-derived macrophages were resistant to GO-triggered necrosis. Similarly, GO did not induce necrosis of HEK293T/TLR4-null cells. Macrophagic cell death upon GO treatment was partially attributed to RIP1-RIP3 complex-mediated programmed necrosis downstream of TNF-α induction. Additionally, upon uptake into macrophages, GO accumulated primarily in cytoplasm causing dramatic morphologic alterations and a significant reduction of the macrophagic ability in phagocytosis. However, macrophagic uptake of GO may not be required for induction of necrosis. GO exposure also caused a large increase of intracellular reactive oxygen species (ROS), which contributed to the cause of cell death. The combined data reveal that interaction of GO with TLR4 is the predominant molecular mechanism underlying GO-induced macrophagic necrosis; also, cytoskeletal damage and oxidative stress contribute to decreased viability and function of macrophages upon GO treatment.

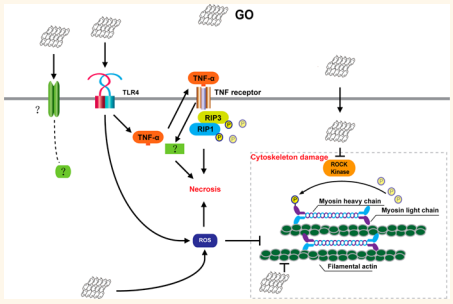

KEYWORDS: graphene · macrophages · necrosis · toll-like receptor 4 · cytoskeleton · oxidative stress

Graphene is a 2D material consisting of a single layer of carbon atoms arranged in a regular hexagonal pattern. Since its discovery in 2004, graphene and its oxidized derivative graphene oxide (GO) have revealed promising applications in biotechnology, biomedicine and electronics.[1−3] For instance, works with biofunctionalized GO (such as PEGylated GO) have demonstrated great potentials in tumor inhibition, drug delivery and biosensing.[2,4] To date, a limited number of studies proposed that GO is biocompatible to mammalian cells;[5−8] however, studies of its potential hazard remain inconclusive because of differences in materials and in experimental methodology.[9,10]

The blood circulation system is an important barrier against the invasion of nanomaterials upon exposure *via* biomedical applications or environmental absorption. Blood cells are primarily responsible for governing their trafficking and systemic translocation. Among blood cells, macrophages are the cardinal cell type in the immune system responding to foreign invaders. On one hand, macrophages can ingest pathogens and destroy them; on the other hand, macrophages are involved in systemic inflammatory response by secreting inflammatory cytokines, and are also associated with antigen presentation to T cells.[11] Several studies have documented the adverse effects of pristine graphene and GO in erythrocytes and platelets of blood cells.[12,13] However, regarding graphene-mediated cytotoxicity in monocyte/macrophage, the current understanding is limited and warrants further detailed investigation.

* Address correspondence to sjliu@rcees.ac.cn.

Received for review January 14, 2013 and accepted June 4, 2013.

Published online June 04, 2013
10.1021/nn402330b

© 2013 American Chemical Society

Although limited studies have suggested graphene's biocompatibility toward macrophages,[14] there are burgeoning data indicating its pro-inflammatory and cytotoxic impact on macrophages such as autophagy or cell death.[15−17] Cell death was initially divided into 2 categories, apoptosis and necrosis, and the latter was considered as a quick and uncontrolled event. However, recent studies have demonstrated that necrosis could also be a concertedly programmed process of cell death under caspase-compromised conditions.[18−20] Programmed necrosis usually, but not always, requires the activation of receptor-interacting protein kinase 1 and 3 (RIP1 and RIP3) in response to a variety of stresses including oxidative stresses, viral infections and DNA damage.[18,21,22]

Toll-like receptor 4 (TLR4) functions as a lipopolysaccharide (LPS) sensing receptor and is the key component within the receptor complex that senses bacterial invaders.[23] Activation of TLR4 signaling results in TNF-α-induced programmed necrosis in macrophages.[20] In this report, we demonstrated that GO induced macrophagic cell death by activating TLR4-dependent programmed necrosis. GO treatment also resulted in massive intracellular reactive oxygen species (ROS) production. Furthermore, GO uptake by macrophages resulted in disruption of cytoskeleton and reduction in the ability of phagocytosis. Together these results establish the mechanisms of cytotoxicity induced by GO in macrophages.

RESULTS

Necrosis of Macrophages Induced by Graphene Derivatives. Three types of graphene derivatives were used to address the biological effect of graphene on macrophages: GO, aminated graphene, and carboxylated graphene with the thickness of about 1 nm and the size of 1 to 2 μm (Figure 1A). All graphene-based nanomaterials used in this work were homogenously dispersed in H_2O and culture medium. The zeta potential of these graphene derivatives indicated that they were all negatively charged in water (Figure 1B). Moreover, these graphene derivatives revealed similar zeta potentials in culture medium (Figure 1B), suggesting their comparable surface charge for them under a biological setting.

We first assessed apoptosis and necrosis of two macrophage cell lines J774A.1 and RAW 264.7 upon exposure to graphene derivatives using flow cytometry (FACS) with fluorescein isothiocyanate (FITC)-conjugated Annexin V and propidium iodide (PI) staining. As shown in Figure 2A, PI^+ necrotic cells were dramatically increased in J774A.1 treated with GO, aminated graphene, or carboxylated graphene ($p < 0.001$), without significant increase of apoptotic cells (Annexin V^+ population). Similar findings were observed in RAW 264.7 cells treated with GO, aminated graphene, or carboxylated graphene (Figure 2A, $p < 0.001$). And a

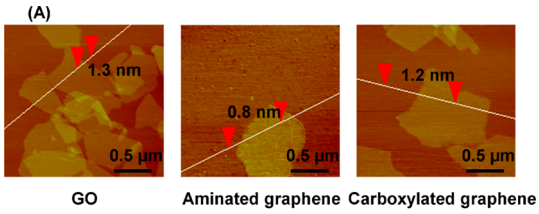

(B)

Graphene	Zeta potential (mV) ±SD	
	In water	In culture medium
GO	-35.3±1.1	-6.0±1.0
Aminated graphene	-19.0±1.3	-5.9±0.3
Carboxylated graphene	-42.8±1.2	-7.2±0.4

Figure 1. Characterization of graphene derivatives. (A) Representative atom force microscopy (AFM) topography images of GO, aminated graphene, and carboxylated graphene. The thickness of GO, aminated graphene, and carboxylated graphene is 1.3, 0.8, and 1.2 nm, respectively, and the size distribution for them similarly ranges from 1 to 2 μm. The arrows in the height profile indicate the thicknesses of graphene sheets. (B) Zeta potentials of GO, aminated graphene, and carboxylated graphene in H_2O and culture medium.

slight difference was found between J774A.1 and RAW 264.7 in response to aminated graphene and carboxylated graphene (Figure 2A). This difference likely resides in the inherent distinct characteristics of these two cell lines,[24,25] which warrants detailed investigation in the future. In addition, to unveil a potentially specific effect of graphene on macrophagic cell death, we used other carbon nanomaterials with different physicochemcial properties from graphene, *i.e.*, nanoparticulate carbon black and fiber-shaped carboxylated multiwall carbon nanotubes (MWCNTs). As shown in Figure 2A, carbon black and MWCNTs did not trigger cell death of both J774A.1 and RAW 264.7 cells.

Necrotic cell death is defined as the PI^+ population without caspase activation as previously described.[18] We then examined activation of caspase-3, a central effector of apoptosis,[26] in J774A.1 cells treated with GO. We observed the full-length caspase-3 only without cleaved caspase-3 (the activated form) (Figure 2B), indicating no apoptosis for these cells. In contrast, staurosporine (STA), which served as a positive control, activated caspase-3 with a significant induction of cleaved caspase-3 in J774A.1 cells (Figure 2B). In agreement with the significant decrease in cell survival observed in both J774A.1 and RAW 264.7 cells, the numbers of viable cells decreased dramatically after 24 and 48 h exposure to GO from 10 to 80 μg/mL (Figure 2C, $p < 0.05$). In addition, GO inhibited proliferation of J774A.1 and RAW 264.7 cells in a dose-dependent manner from 2.5 to 80 μg/mL for 48 h ($p < 0.001$), as determined by the BrdU incorporation assay (Figure 2D). Interestingly, we did not observe any impairment to cell growth and survival of other cell types including mouse Hepa 1−6 hepatocytes, human

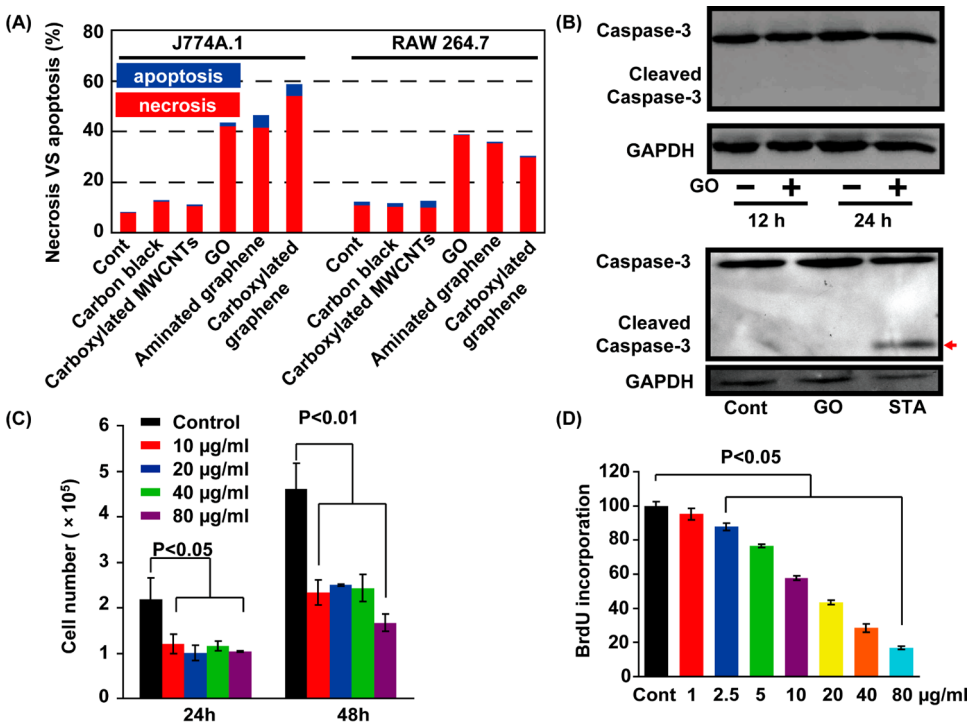

Figure 2. Reduced cell survival of macrophages exposed to graphene derivatives. (A) Proportions of necrosis and apoptosis in J774A.1 and RAW 264.7 cells. Cells were treated with carbon black, carboxylated MWCNTs, GO, aminated graphene or carboxylated graphene at 40 μg/mL for 24 h, and were then collected for FACS analysis of apoptosis and necrosis with FITC-conjugated Annexin V and PI staining. The segment in red for each bar refers to the proportion of necrosis, and the segment in blue for each bar represents the proportion of apoptosis. There were 3 replicates for each group (n = 3), and a set of representative data was shown in stack column chart. (B) Western blot analysis of caspase-3 activation in J774A.1 cells with GO treatment at 40 μg/mL for 12 or 24 h. STA at 1 μM was used to activate caspase-3. The red arrow indicates the location of cleaved caspase-3. (C) Cell numbers and (D) BrdU incorporation were determined in cells after exposure to GO at 10, 20, 40, and 80 μg/mL for 24 and 48 h for cell number counting and 48 h for the BrdU incorporation assay (n = 6).

Hepa G2 hepatocytes, or human MB-MDA-231 breast cancer cells upon graphene treatment at similar concentrations (data not shown). Importantly, we demonstrated that the concentrations of endotoxin for all graphene suspensions were about 0.1 EU/mL, less than the threshold of 0.25 EU/mL,[27] demonstrating no significant endotoxin contamination in graphene samples used in our study. These data excluded the possibility of adverse effects of endotoxin on macrophages.

Together, these data demonstrated that these graphene derivatives impaired cell growth and caused necrotic cell death in J774A.1 and RAW 264.7 macrophages. Among the 3 types of graphene derivatives, GO induced necrosis to a similar extent in both J774A.1 and RAW 264.7 cells (Figure 2A). Because GO could be used as a fundamental building block for further functionalization, such as carboxylated or amine modified graphene and other graphene derivatives,[3,28,29] we therefore selected GO to embark on the mechanisms underlying graphene-induced necrosis on macrophages.

TLR4-Dependent Programmed Necrosis of Macrophages upon GO Exposure. Recent studies have suggested a possible interaction between TLR and graphene, which is likely responsible for graphene-induced effects on macrophages.[17,30] Moreover, a recent study demonstrated that heme-mediated activation of TLR4 signaling resulted in substantial ROS generation and TNF-α secretion, leading to programmed necrosis on macrophages in a ROS- and autocrine TNF-dependent manner.[21] Programmed necrosis can be initiated by the ligation of tumor necrosis factor receptor (TNFR) and the formation of a RIP1-RIP3 complex (necrosome).[19,23] To study whether TLR4 and its downstream molecules were involved in GO-induced macrophagic necrosis, we used a selective TLR4 signaling inhibitor (CLI-095) to block the TLR4 signaling. After 3-h exposure of J774A.1 cells to GO (40 μg/mL), more than 45% of cells underwent necrosis in comparison to less than 15% of the untreated control cells ($p < 0.001$). Most importantly, pretreatment of cells with the TLR4 signaling inhibitor CLI-095 (1 μg/mL) dramatically decreased cells death, as the percentage of necrotic cells was at a comparable level to that in control cells ($p < 0.001$) (Figure 3A). To further establish the role of TLR4 in GO-provoked necrosis, we examined cell death in bone marrow derived-macrophages (BMDMs) derived from TLR4-deficient ($TLR4^{-/-}$) and wild-type (wt) mice. Since primary macrophages were more sensitive to GO than J774A.1 and RAW 264.7 cells, BMDMs were exposed to a lower concentration of GO (20 μg/mL). As shown in

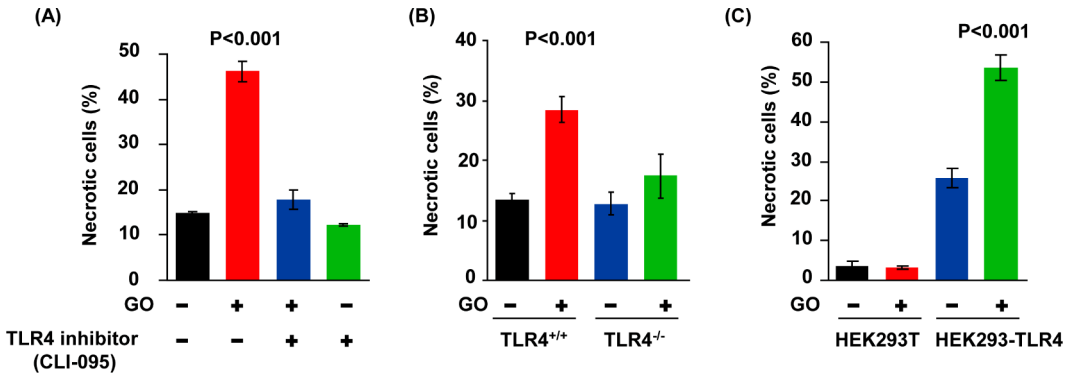

Figure 3. GO induced macrophagic cell death through programmed necrosis. (A) Percentages of necrosis in J774A.1 cells upon exposure to 40 μg/mL GO for 3 h in the presence or absence of TLR4 signaling inhibitor CLI-095. (B) Proportions of necrosis in wt or *TLR4*$^{-/-}$ BMDMs upon treatment with GO at 20 μg/mL for 3 h. (C) Necrosis in TLR4-null HEK293T and HEK293/TLR4 upon exposure to 40 μg/mL GO for 3 h.

Figure 3B, GO greatly promoted necrosis of wt BMDMs after 3-h exposure to GO; in contrast, *TLR4*$^{-/-}$ BMDMs were resistant to GO treatment. Additionally, we investigated the cell death of HEK293T cells with no endogenous expression of TLR4 (TLR4-null) and HEK293/TLR4 cells which were obtained by stable transfection of murine TLR4 gene.[31] GO exerted little effect on HEK293T/TLR4-null cells with no induction of cell death; in contrast, GO greatly provoked necrosis of HEK293/TLR4 cells by more than 2-fold compared to untreated cells (Figure 3C, $P < 0.001$). These results together indicated that TLR4 was necessary for GO-induced necrosis. Wei and colleagues recently demonstrated that the bending stiffness of graphene is similar to that of lipid bilayers of cells,[32] which might highlight the molecular basis for the interaction between graphene and biomolecules on cell membrane, such as proteins. To this end, we would assume that the fundamental physicochemcial properties (*e.g.*, bending rigidity and bending stiffness) would account for a possible interaction between graphene and TLR4.

Since proinflammatory cytokines from macrophages are stimulated upon TLR4 activation by its ligand, such as LPS, we therefore assessed TNF-α expression in cells upon GO exposure. The induction of TNF-α mRNA was >10 fold in cells treated with GO at 40 μg/mL ($p < 0.001$, Figure 4A), similar to results from previous studies.[17,30] Concomitantly, the protein level of TNF-α secreted into culture medium was substantially increased in cells treated with GO as determined by ELISA (Figure S1, $p = 0.001$). However, this induction of TNF-α was largely prevented by pretreatment with the TLR4 signaling inhibitor (Figure 4A, $p < 0.001$). The inhibitor itself had no significant effects on cell death and TNF-α expression (Figure 4A). It has been shown that TNF-α-induced programmed necrosis of macrophages is often dependent on activation of the RIP1/RIP3 complex.[33] RIP3 phosphorylation results in formation of a tight RIP1-RIP3 complex and further activation of the complex, leading to initiation of the necrotic program.[34,35] As shown in Figure 4B, RIP3 was phosphorylated in cells upon GO treatment, and the increased phosphorylation of RIP3 could be attenuated by pretreatment with the TLR4 inhibitor. In addition, an antagonist of TNF-α/TNF-α receptor (TNFR), the WP9QY peptide,[36] was used to block the action of TNF-α on TNFR. There was approximately 50% reduction of necrosis for cells simultaneously treated with GO and the WP9QY peptide, compared to cells treated with GO only (Figure 4C, $P < 0.001$), demonstrating that autocrine TNF-α was necessary to initiate necrosis in macrophages. These data suggested that TLR4-dependent TNF-α induction and RIP1/3 activation downstream of TNF-α were likely the molecular basis underlying macrophagic necrosis challenged by GO.

It has been reported that TNF-α elicits programmed necrosis mainly but not exclusively through the activation of kinases RIP1 and RIP3.[33,37−41] We also tested the efficacy of a RIP inhibitor necrostatin-1 (NEC-1, specifically targets RIP1/RIP3)[42] in preventing GO-induced necrosis in macrophages. Pretreatment with NEC-1 could significantly rescue J774A.1 cells from necrosis with 43% reduction ($P < 0.001$), and NEC-1 itself has little effect on cell death (Figure 4D). However, NEC-1 pretreatment could not reduce necrosis to the basal level as that in the control, consistent with the previous findings that additional pathways of necrosis independent of RIP1/RIP3 may be involved.[38−41]

These results together demonstrated that GO promoted cell death of macrophages predominantly through programmed necrosis, which was closely dependent on the activation of TLR4 signaling, TNF-α secretion, and TNF-α initiated programmed necrosis that involved RIP-dependent and -independent signaling pathways.

GO's Cellular Uptake and GO-Induced Morphological Alterations in Macrophages. We observed pronounced morphological alterations of J774A.1 cells exposed to 20 μg/mL GO for 24 h (Figure 5A). There was a large collapse in cellular body (as shown by arrows in Figure 5A), leading

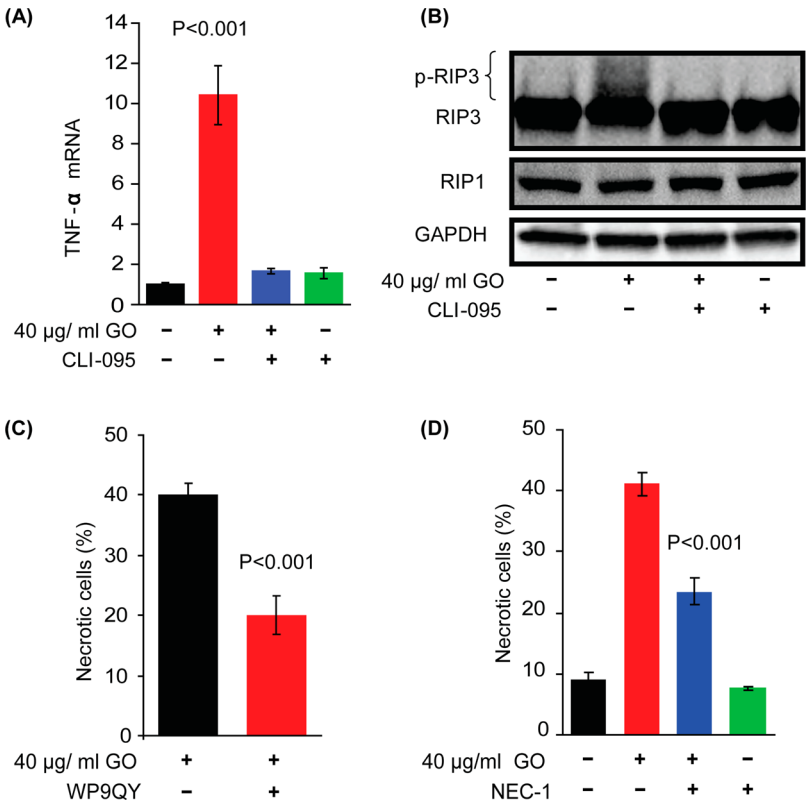

Figure 4. Activation of TNF-α-RIP1/3 signaling upon GO treatment. (A) TNF-α expression in J774A.1 cells exposed to GO for 3 h in the presence or absence of TLR4 inhibitor. (B) Western blot analysis of RIP1/3 in J774A.1 cells treated or untreated with GO for 3 h in combination with pretreatment of TLR4 inhibitor. (C) Proportions of necrotic J774A.1 cells upon exposure to 40 μg/mL GO for 3 h with or without pretreatment of an antagonist of TNF-α/TNFR, the WP9QY peptide. (D) Percentages of necrosis in J774A.1 cells treated with GO for 3 h with or without pretreatment of NEC-1.

to a significant increase of cell size (~1.6-fold, $p < 0.01$) (data not shown). To further delineate the site of collapse, we stained cytoskeleton with FITC-conjugated phalloidin (green) and nuclei with 4′,6-diamidino-2-phenylindole (DAPI, blue).[43] As shown in Figure 5B, collapse occurred within cytosolic compartment, which caused nuclei to move to the periphery of cell membrane. There was significant disassembly of actin fibers with a considerable reduction in the density of actin meshwork in cells upon GO treatment compared to the control cells (Figure 5B). Moreover, the macrophagic characteristic structure of cells, surface protrusion, was also remarkably affected in J774A.1 cells treated with 20 μg/mL GO for 24 h; the number of surface protrusions and their actin intensity were greatly reduced by approximately 30% and 35%, respectively (Figure 5B and data not shown, $p < 0.01$). In agreement with these results, the cytoskeletal disruptive effect coupled to cell death was also reported for hydroxylated fullerene ($C_{60}OHx$).[44]

To further investigate the correlation between cytoskeletal disruption and GO exposure to cells, we localized GO inside cells by the confocal microRaman spectroscopy. A representative J774A.1 cell exposed to GO at 40 μg/mL for 24 h with the morphology of a large collapsed area within the cytoplasmic region was chosen for the Raman mapping. The merged image of the Raman mapping with its corresponding bright-field morphological image is shown in Figure 5C. For this study, graphite lattice (G band) at 1577 cm^{-1} and the disorder band (D band) at 1351 cm^{-1} specifically represented GO. The Raman spectra were acquired on 3 target points. Point 1 and 2 were located on the core and the boundary (underneath the cell membrane) of the collapsed area within the cytoplasmic compartment, respectively, and point 3 was randomly selected on a site outside the cell (Figure 5C). There was considerable GO accumulation within the collapse area as evidenced by the enhanced Raman intensity for point 1 as indicated in Figure 5C, suggesting that GO's localization correlated to cellular morphological alterations and cytoskeletal damage. Lower Raman intensity was detected on the border area of the collapse, a site directly underneath the cell membrane (point 2) when compared to that of point 1. Importantly, no Raman signal was detectable outside the cell, demonstrating an excellent signal-to-noise ratio. In addition, GO was also visualized within cytoplasm using transmission electronic microscopy (TEM) (Figure S2). These observations indicated that GO predominantly accumulated in the core of the cytosolic region, and that only a small portion of GO was localized on the border of cytoplasm, consistent with the occurrence

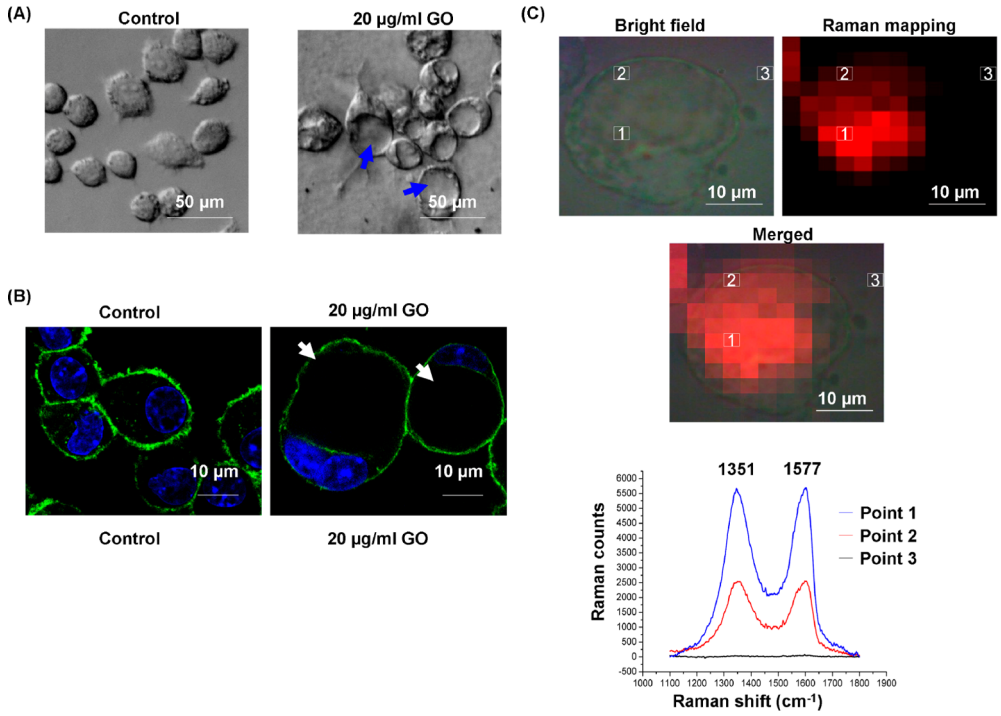

Figure 5. Morphological alterations of cells and characterization of intracellular GO. (A) GO-induced morphological alterations of J774A.1 cells at 20 μg/mL for 24 h. Arrows indicate the collapsed areas. Original magnification, $\times$200. (B) Cytoskeleton staining with FITC-conjugated phalloidin (green) and nuclear staining with DAPI (blue) in cells upon GO 20 μg/mL treatment for 24 h. Two colors are merged together. Arrows indicate the collapse areas. Original magnification, $\times$400. (C) Raman mapping based on the intensity of D band at 1351 cm cm^{-1} of the chosen J774A.1 cell with the representative morphology of a large collapsed area in response to GO at 40 μg/mL for 24 h. The Raman image is merged with its corresponding bright-field image. Specific Raman spectrum was acquired from 3 target points. Point 1 and 2 were located on the core and the boundary (underneath cell membrane) of the collapse area within the cytoplasmic region, respectively, and point 3 was randomly selected on an acellular area outside the cell. Graphite lattice (G band) at 1577 cm^{-1} and the disorder band (D band) at 1351 cm^{-1} are characteristic Raman signatures of GO.

of cell membrane collapse coupled to cytoskeletal disruption.

GO-Induced Morphological Changes Required the Internalization of GO into Macrophages. To further investigate our hypothesis that GO-induced morphological alterations to macrophages were dependent on its internalization and intracellular accumulation, we looked into uptake of FITC-bovine serum albumin (BSA) labeled GO by macrophages characterized by FACS and corresponding morphological changes of macrophages during the time course from 30 min to 24 h. As shown in Figure 6A, there was an apparent time-dependent increase of intracellular GO accumulation from 30 min to 24 h for both J774A.1 cells and RAW 264.7 cells upon exposure to 40 μg/mL FITC-BSA labeled GO ($p < 0.001$). Macrophages were also incubated with the supernatant of FITC-BSA-GO spin-down solution after pelleting FITC-BSA-GO; however, no intracellular fluorescence was detected (data not shown). Moreover, no intracellular fluorescence could be observed after incubation with FITC-BSA solution only (data not shown). These findings demonstrated that the intracellular fluorescence was solely attributed to the uptake of FITC-BSA-GO. Although this method was not a perfect approach to determine the absolute amount of GO engulfed by macrophages, it could appropriately reflect the kinetic uptake of GO. We observed membrane collapse starting at 3 h after GO treatment, but not at earlier time points such as 1 h. More dramatic phenotype was observed after 6 h (Figure 6B), suggesting that morphological alterations of macrophages closely followed GO's uptake.

To further validate the effect of GO internalization on macrophagic morphological alterations, we performed exposure experiments in *Hri*$^{-/-}$ BMDMs, which were demonstrated to have significant deficiency in phagocytosis.[45] It has been demonstrated that *Hri*$^{-/-}$ BMDMs have reduced ability in phagocytosis due to attenuated macrophagic differentiation,[45] we thus selected this cell model to study the role of macrophagic uptake of GO in morphological changes and necrosis induction. Indeed, there was a significant difference in the morphological changes between wt and *Hri*$^{-/-}$ BMDMs after exposure to 20 μg/mL GO even for 3 h (Figure 7A). Numerous wt BMDMs harbored large collapses within the cellular body; in contrast, only a few *Hri*$^{-/-}$ BMDMs displayed this morphological change (as shown by arrows in Figure 7A). After GO exposure for 24 h, most wt BMDMs displayed dramatic morphological changes with membrane collapses and increased

cellular volume (about 70% increase, $p < 0.05$); while, $Hri^{-/-}$ BMDMs exhibited mild changes with fewer membrane collapses and a smaller cellular volume change (about 7% increase) than wt BMDMs (Figure 7A). We also assessed the intracellular accumulation of GO in wt and $Hri^{-/-}$ BMDMs after exposure to 20 μg/mL FITC-BSA labeled GO for 24 h. Uptake of GO into BMDMs as measured by the proportion of GO-laden cells was reduced by approximately 40% with *Hri* deficiency (Figure 7B, $p < 0.05$), indicating a significant reduction of GO internalization in $Hri^{-/-}$ BMDMs compared to wt cells. No significant difference in necrosis was found between wt and $Hri^{-/-}$ BMDMs upon GO treatment at different time points (such as at 12 h shown in Figure 7C), suggesting diminished GO internalization could not sufficiently impede cell death. Meanwhile, pretreatment of cells with the TLR4 signaling inhibitor could not prohibit morphological changes of macrophages induced by GO (data not shown). These data clearly demonstrated that GO-mediated morphological alterations to macrophages were largely attributed to internalization of GO, and the absence of *Hri* could significantly relieve the morphological impairments due to reduced phagocytosis of GO in these cells.

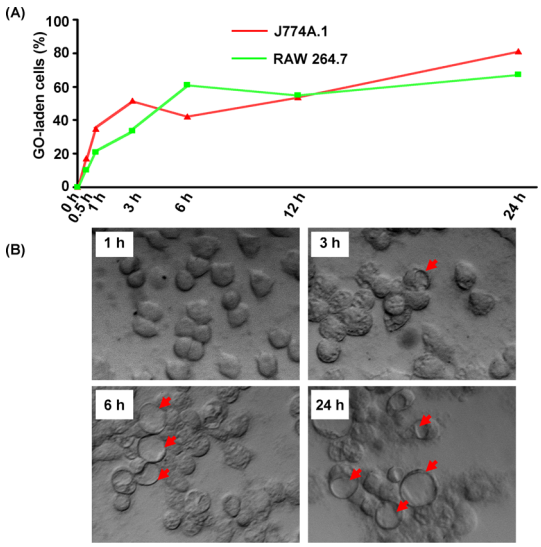

Figure 6. Determination of intracellular GO accumulation and morphological alterations. (A) FACS analysis of GO-laden J774A.1 and RAW 264.7 cells after exposure to FITC-BSA labeled GO at 40 μg/mL at different time points as indicated (n = 3). (B) Representative images of corresponding morphological alterations of J774A.1 cells. Arrows indicate the collapsed areas. Original magnification, ×200.

GO-Mediated Inhibition on ROCK Activity and Macrophagic Phagocytosis. The Rho family of small GTPases plays a central role in controlling cell morphology and motility, and ROCK is the principal mediator of Rho activity.[46−48] ROCK governs the fundamental organization and dynamics of actin cytoskeleton by phosphorylating a number of downstream targets.[48] Dampened ROCK activity leads to attenuation in globular actin polymerization, assembly of filamentous myosin heavy chain, and the binding between myosin and

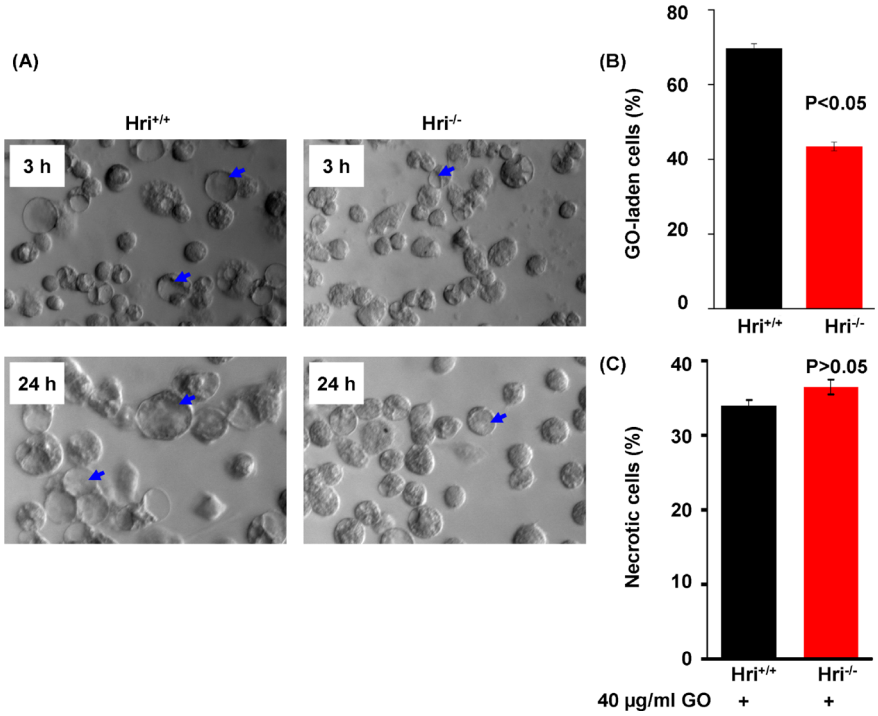

Figure 7. Morphological alterations and cell death of BMDMs upon GO treatment in Hri deficiency. (A) Representative images of GO-induced morphological alterations of wt and $Hri^{-/-}$ BMDMs at 20 μg/mL for 3 and 24 h. Arrows indicate collapsed areas. Original magnification, ×200. (B) FACS analysis of GO-laden wt and $Hri^{-/-}$ BMDMs after exposure to FITC-BSA labeled GO at 20 μg/mL for 24 h (n = 3). (C) Proportions of necrosis in $Hri^{+/+}$ and $Hri^{-/-}$ BMDMs after exposure to 40 μg/mL GO for 12 h.

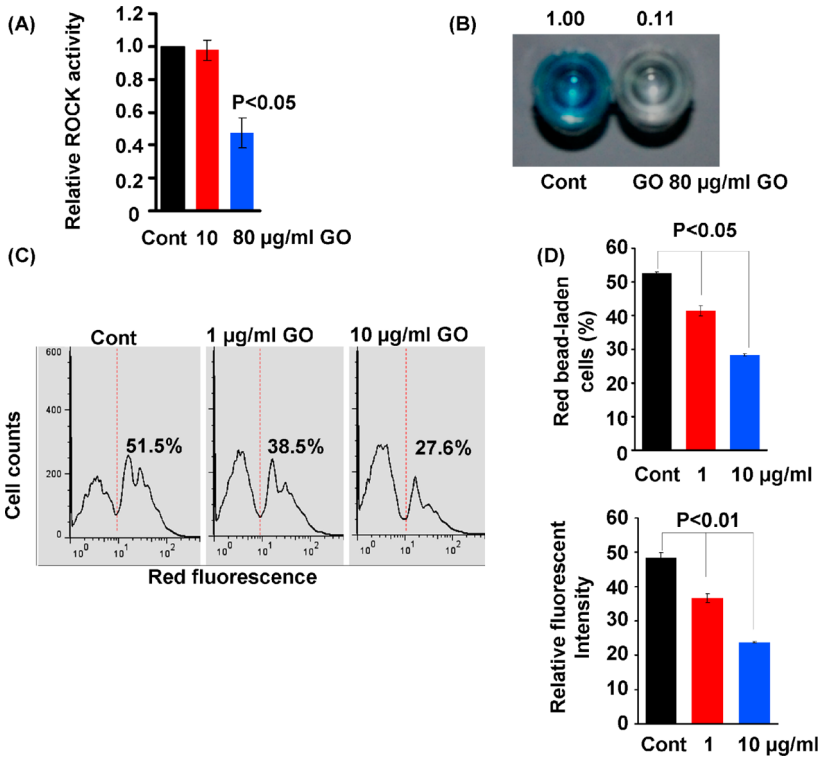

Figure 8. GO impaired cellular ROCK activity and the macrophagic function. (A) ROCK activity in cells upon GO treatment at 10 and 80 μg/mL for 24 h ($n = 3$). (B) Acellular ROCK activity assay. Two representative wells with corresponding relative values are shown. (C) GO attenuated the ability of phagocytosis. Representative images from the FACS analysis of J774A.1 cells engulfing red beads after GO treatment at 1 and 10 μg/mL for 24 h. (D) The average percentage of cells containing red beads, and the relative fluorescent intensity in red bead-laden cells ($n = 6$).

filamentous actin (F-actin).[48] As shown in Figure 8A, ROCK activity was decreased significantly in J774A.1 cells upon GO treatment at 80 μg/mL (reduction by 53%, $p < 0.05$) for 24 h compared to the control. The results from the acellular kinase assay also demonstrated that GO had a direct inhibitory effect on ROCK activity (Figure 8B). Thus, we concluded that reduced ROCK activity after exposure to GO was correlated with a loss in the organization of the cytoskeletal scaffold and morphological alterations in macrophages.

Since macrophage plays a critical role in clearing foreign invaders by phagocytosis, decreased cell viability, induced cell death, and reduced integrity of actin cytoskeleton upon GO treatment (shown above) might significantly impair macrophagic ability in phagocytosis. Phagocytosis was quantified by the ingestion of the amine-modified latex beads in J774A.1 cells. To better evaluate the effect of GO treatment on macrophagic function, we chose lower concentrations of GO to avoid dramatic cell death in the following experiments. The FACS results showed that the percentage of cells containing beads was reduced by approximately 25% and 47% upon 1 and 10 μg/mL GO treatment, respectively, compared to the control (Figure 8C,D, $p < 0.05$). Furthermore, the relative intensity of the intracellular red fluorescence in bead-laden cells was reduced in GO-treated cells (by 21% and 31% for 1 and 10 μg/mL treatment, respectively) in comparison to the control (Figure 8D, $p < 0.01$), indicating that the number of red fluorescent latex beads was fewer in GO-treated cells than that in control cells. These results demonstrated that the macrophagic ability in phagocytosis was significantly dampened upon exposure to GO, and this reduced phagocytosis was likely due to GO-induced damage to cytoskeleton and also cell viability as described above.

GO Induced Oxidative Stress to Macrophages. Since activation of TLR4 signaling and uptake of foreign particles into macrophages could trigger oxidative stress,[49−51] we thus measured intracellular ROS content in macrophages after GO treatment. There was a significant increase in ROS levels as measured by DCF fluorescence upon GO treatment over time from 10 min to 6 h (Figure 9A, $p < 0.05$). Even only for 10 min at a low concentration of 10 μg/mL, the DCF fluorescence increased about 1.8-fold in J774A.1 cells treated with GO compared to the control (Figure 9A, $p < 0.001$). Additionally, there was a dramatic increase of the DCF fluorescence as GO concentration increased from 10 to 80 μg/mL ($p < 0.001$, Figure 9A). A similar intracellular ROS generation profile induced by GO was also observed in RAW 264.7 cells (Figure 9A).

We also determined mitochondrial superoxide production in GO-treated cells using MitoSOX red with FACS. MitoSOX red is a novel fluorogenic indicator

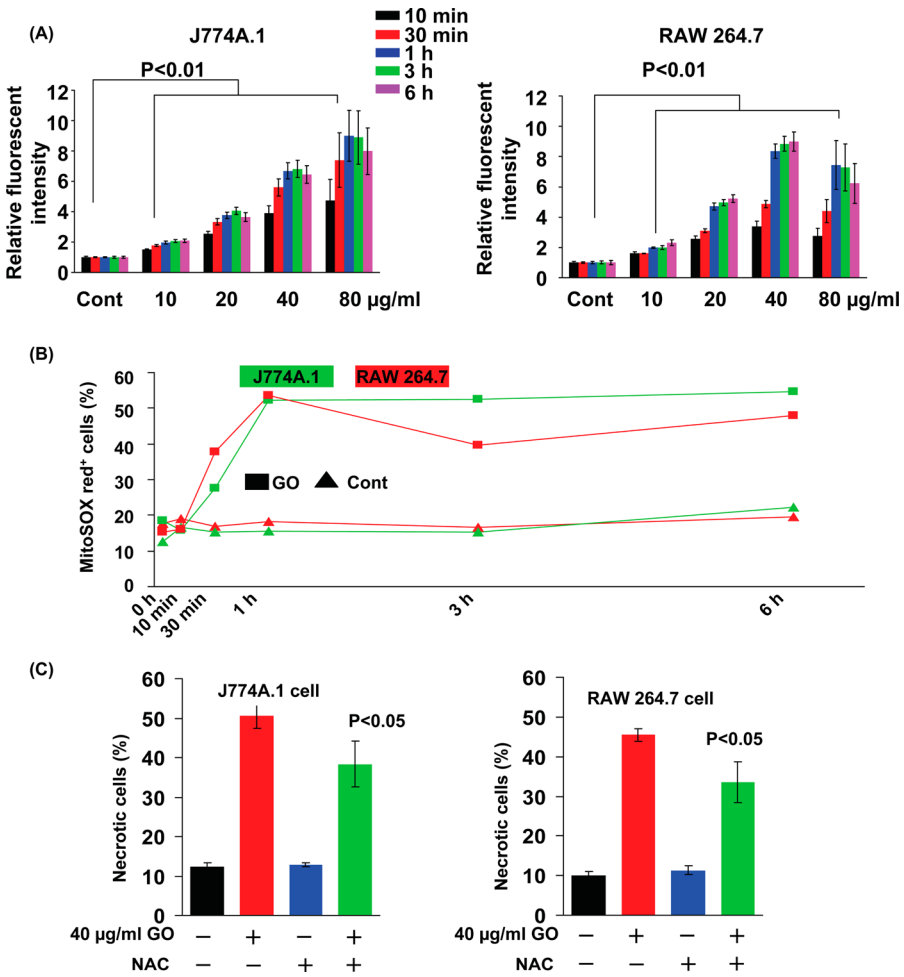

Figure 9. GO induced oxidative stress in macrophages. (A) Relative DCF fluorescent intensities reflecting the intracellular ROS generation upon GO treatment at various concentrations at different time points in J774A.1 cells and RAW 264.7 cells ($n = 6$). (B) Mitochondrial superoxide assay in J774A.1 and RAW 264.7 cells in response to GO at 40 μg/mL at different time points as indicated ($n = 3$). (C) Proportions of necrotic cells upon removal of intracellular ROS. J774A.1 and RAW 264.7 cells were treated with GO at 40 μg/mL for 3 h with or without pretreatment of NAC ($n = 6$).

for measuring superoxide (O_2^-) in mitochondria of live cells, and is also used to determine the level of oxidative stress triggered by nanomaterials.[52,53] As shown in Figure 9B, GO caused a significant time-dependent increase of MitoSOX red-positive cells from 30 min to 6 h after exposure to 40 μg/mL GO for both J774A.1 and RAW 264.7 cells ($p < 0.001$). To substantiate the role of oxidative stress in eliciting necrosis of macrophages by GO, we pretreated cells with *N*-acetyl cysteine (NAC), an antioxidant.[54,55] ROS production was significantly undermined by NAC pretreatment with >35% reduction in both J774A.1 and RAW 264.7 cells treated with GO at 40 μg/mL, compared to cells without pretreatment of NAC. In the meantime, however, cell death was greatly ameliorated upon pretreatment of NAC, as the proportion of necrotic cells decreased >20% compared to cells without pretreatment of NAC for both J774A.1 and RAW 264.7 (Figure 9C, $P < 0.05$). In short, oxidative stress was demonstrated to be an important modulator (to a less extent than TLR4-dependnet effects) of macrophagic necrosis induced by GO.

DISCUSSION

The shape of nanomaterials is one of the essential determinants of their biological effects.[56−58] Graphene is a one-atom-thick planar sheet of SP2-bonded carbon atoms, and it displays novel biological effects with distinct structure−activity relationships.[59] In this report, we compared several carbon-based materials, and found that graphene derivatives (*i.e.*, GO, aminated graphene, and carboxylated graphene) greatly induced necrosis of macrophages; in contrast, carbon black and carboxylated MWCNTs did not induce cell death, suggesting that the 2D structure of graphene could play a critical role in mediating this effect. Larger pieces of graphene might not be engulfed by macrophages, but could be absorbed to cell membrane and interact with membrane proteins.[60] In parallel to our results, a recent study demonstrated a close bending stiffness of graphene to that of lipid bilayers of cells,[32] supporting the notion that the basic physicochemcial properties (such as bending rigidity and bending stiffness) could determine the close interaction between

nanomaterials and membrane proteins.[61−63] Smaller graphene with sharp edges, however, could be engulfed by macrophages to interact and possibly to cut actin filaments, resulting in disruption of cytoskeleton.[62,64] We here demonstrated that GO elicited programmed necrosis on macrophages primarily through TLR4-dependent signaling. We also demonstrated that GO exposure impaired the integrity of cytoskeleton and promoted massive ROS generation, which reduced cell viability and undermined macrophagic morphology and functions.

In addition to caspase-dependent apoptosis, programmed necrosis, namely necroptosis, is another crucial type of cell death that can occur through embryonic development and under various stresses.[19,21,22] Many stimuli elicit programmed necrosis, such as TNF, Fas ligand, and microbial engagement on TLRs.[19,21,22] We demonstrated that GO sensitized macrophages to death predominantly through necrosis; moreover, GO-induced necrotic process largely required its interaction with TLR4. Blockade of TLR4 signaling with a selective TLR4 inhibitor CLI-095 could nearly completely preclude cell death. Moreover, absence of TLR4 in *TLR4*-deficient BMDMs endowed these cells with resistance to GO-triggered necrosis. In contrast, gain of TLR4 in TLR4-null HEK293 cells predisposed HEK293/TLR4 cells to necrosis induced by GO. In support of these findings, we have also recently demonstrated that GO could instigate cell death of TLR4-null nonphagocyte erythroid cells prominently through apoptosis but not necrosis,[65] similar to a study demonstrating that graphene stimulated ROS generation and induced cell death *via* apoptosis in PC12 cells (a cell line derived from a pheochromocytoma of the rat adrenal medulla).[10] Increased TNF-α secretion upon activation of TLR4 pathway by GO triggered programmed necrosis through initiating the RIP1/3-centered signaling machinery, and blockade of TNF-α/TNFR with an antagonist could substantially diminish GO-induced necrosis. These results depicted an autocrine TNF-dependent way in response to GO exposure, similar to the findings from a recent study of heme-induced programmed necrosis on macrophages through autocrine TNF.[21] Recent studies have demonstrated that the inflammatory cytokine TNF-α provokes programmed necrosis mainly through the activation of kinases RIP1 and RIP3.[18,21,22] Inhibition of RIP1/RIP3 with a selective inhibitor NEC-1 could not completely prevent necrosis of macrophages upon GO treatment, in agreement with recent findings that additional pathways could also contribute to programmed necrosis independent of RIP1 in the context of TNF signaling or other signaling pathways.[38−41]

Furthermore, we found that GO exposure caused significant oxidative stress reflected by massive ROS production in macrophages, consistent with previous studies.[10,17,66] Removal of intracellular ROS through pretreatment with NAC could significantly (not completely) prevent necrosis of macrophages. For cells under necrosis, ROS exacerbated cell death progression in various ways such as peroxidation of biomolecules and ATP depletion.[22] Thus, oxidative stress is believed to play a contributive role in TLR4-dependent macrophagic necrosis induced by GO. Meanwhile, pretreatment of NAC did not ameliorate GO-induced morphological alterations to macrophages (data not shown). Since GO's intracellular localization resulted in a very pronounced phenotype of morphological alterations to macrophages, the role of oxidative stress in the cytoskeletal effects was not significant.

Intracellular accumulation of GO led to significant impairment of cytoskeleton as evidenced by cell membrane collapse and reduced macrophagic ability in phagocytosis. Consistent with our results, a recent study demonstrated that pristine graphene could also disrupt F-actin remodeling and impair phagocytosis of RAW 264.7 macrophages.[14] Intriguingly, we found that *Hri*-deficient macrophages were resistant to morphological alterations in that these macrophages had a significantly reduced ability to engulf GO particles compared to wt macrophages. We mechanistically demonstrated that GO treatment restrained ROCK activity with a resultant reduction of actin polymerization and damage to the cytoskeletal meshwork. Actin filament-based cytoskeleton forms a basic scaffold for cells, and cytoskeleton plays a primary role in maintaining cell shape, enabling cellular motion, guiding intracellular transport, regulating cell division, and conducting phagocytosis.[67] Disruption of cytoskeletal meshwork could promote cell death process,[66−68] and could also significantly blunt the macrophagic phagocytic activity.[69,70] Reduced ability of phagocytosis for macrophages in response to GO treatment should be due to the combinatory/synergistic effects of intracellular internalization-induced impairments to cytoskeletal meshwork and a loss of cell viability upon activation of TLR4 signaling. Based on the data from Hri-deficient BMDMs, GO uptake may not be required for necrosis induction. Nonetheless, the biological effects of GO determined by its basic physicochemcial properties, the interaction between GO and biological molecules, and the relationship among TLR4 signaling activation, cytoskeletal damage, and oxidative stress warrant further detailed investigation.

CONCLUSIONS

This study deciphers the molecular mechanisms responsible for GO-induced TLR4-dependent necrosis on macrophages. Interaction of GO with TLR4 results in activation of TLR4 signaling, which is the predominant molecular basis for GO-mediated macrophagic necrosis. Additionally, GO's interaction with TLR4 and its

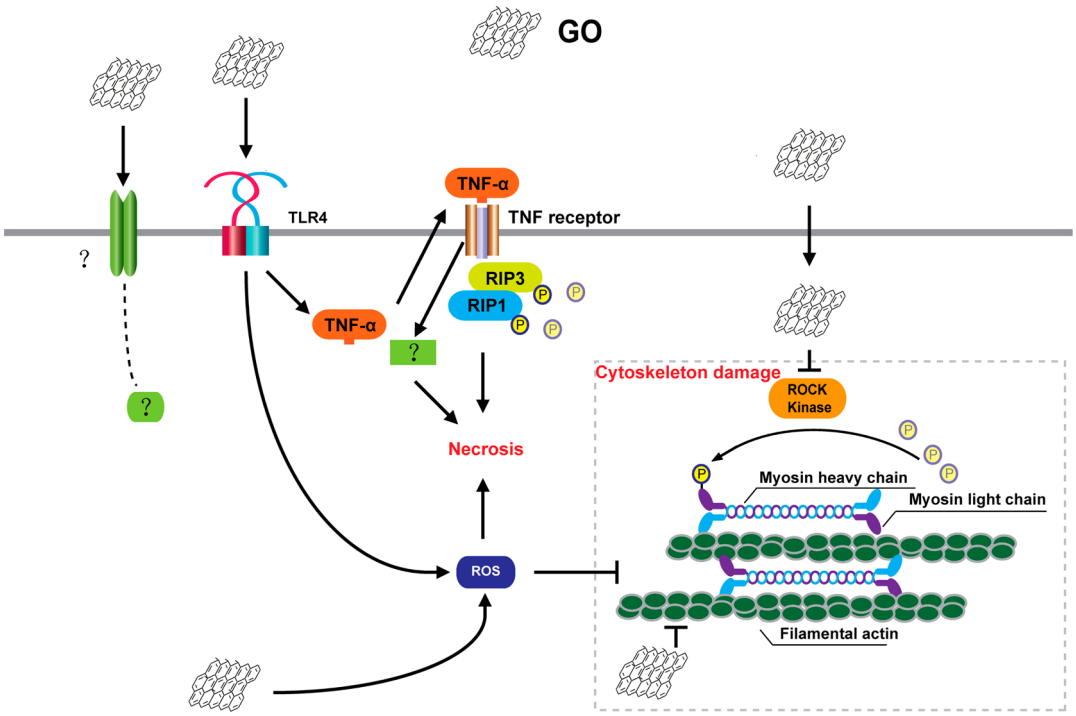

Figure 10. A schematic diagram elucidating the mechanisms responsible for GO-induced cytotoxicity to macrophages. The interaction between GO and TLR4 induces TNF-α production, which triggers programmed necrosis on macrophages in an autocrine loop. Moreover, GO's intracellular localization leads to impairments to macrophagic morphology and function associated with oxidative stress and cytoskeletal disruption. All these together caused significant cytotoxicity and even cell death to macrophages. Additional pathways might also be involved in the regulation of GO-induced cytotoxicity, such as TNF-α-independent signaling and RIP-independent events in initiating programmed necrosis, which warrants future investigations.

intracellular accumulation are associated with oxidative stress and cytoskeletal damage, and these events contribute to decreased viability and function of macrophages. A proposed schematic delineating the mechanisms underlying GO-induced cytotoxicity to macrophages is illustrated in Figure 10.

MATERIALS AND METHODS

Nanomaterial Preparation and Characterization, and Endotoxin Detection. GO was synthesized using the Hummers method with minor revisions as previously described.[71] Aminated graphene and carboxylated graphene were purchased from JCNANO (Nanjing, China). These nanomaterials were characterized with the AFM assessment by a Veeco Dimension 3100 scanning probe microscope (Plainview, NY). Zeta potential of graphene was measured at 20 μg/mL by a laser particle size analyzer (Malvern Nano ZS, Nalvern, U.K.). The suspensions for each graphene derivative were diluted to 0.5 mg/mL in endotoxin-free PBS for further experiments. Carbon black (Printex 90) was obtained from Degussa (Hanau, Germany). Carboxylated MWCNTs were prepared as previously described,[72] with an average diameter of 40 nm and an average length of 0.5−5 μm. Carbon black (Printex 90) and MWCNTs were diluted to 1 mg/mL in endotoxin-free PBS for experiments. Regarding the detection of endotoxin, graphene suspensions were spun down after dilution with endotoxin-free PBS for 4 days, and the supernatants were subjected to endotoxin test with a Limulus Amebocyte Lysate (LAL) kit from Lonza.

Animal Strains and Maintenance. All animal care and surgical procedures were approved by the Animal Ethics Committee at the Research Center for Eco-Environmental Sciences, Chinese Academy of Sciences. TLR4-deficient mice (C57BL/10ScNJ) were maintained in the animal facility at Nanjing University, Nanjing, China. *Hri*$^{-/-}$ mice were generated and maintained as described previously.[45] Genotyping was assessed by PCR using tail DNA. The PCR reaction was similar to that previously described.[45] *Hri*$^{-/-}$ mice were under the C57BL/6J genetic background. Wt mice under the same genetic background as *TLR4*$^{-/-}$ or *Hri*$^{-/-}$ mice were used.

Cell Culture and Treatments. Mouse J774A.1 and RAW 264.7 macrophages, HEK293T cells, mouse Hepa 1−6 hepatocytes, human MB-MDA-231 breast cancer cells and HepG2 hepatocellular liver carcinoma cells were purchased from the Shanghai Cell Bank of Type Culture Collection of China. HEK293/TLR4 cell line was purchased from InvivoGen (San Diego, CA). Cell morphology was imaged under a phase-contrast microscope. The relative cellular flat surface area was measured with Image-Pro-Plus software (Media Cybernetics). Regarding experiments of blockade of TLR4 signaling, a selective TLR4 signaling inhibitor (CLI-095, InvivoGen) was used to pretreat cells overnight prior to GO exposure at an application concentration of 1 μg/mL. To block the TNF-α/TNFR signaling, the WP9QY peptide (Abgent), an antagonist of TNF-α/TNFR, was used to pretreat cells at 50 μM overnight prior to GO treatment. To inhibit RIP activity, cells were pretreated with 30 nM of NEC-1 (necrostatin-1, Sigma) overnight before GO exposure.

BMDMs were isolated and cultured as previously described.[33,53] In brief, femurs and tibias were removed from 6-week-old male mice, and then bone marrow cells were flushed into 1.5 mL tubes. After washing twice with PBS plus 2% FBS, all cells were cultured in DMEM with high glucose, glutamine, 15% heat-inactivated FBS, 25 ng/mL rmCSF-1 (PeproTech), nonessential amino acids (Cambrex), penicillin/streptomycin (Invitrogen), and

55 nM β-mercaptoethanol (β-ME, Sigma-Aldrich) for 3 days. Nonmacrophage cells were then washed off with PBS, and medium was changed every day until day 7. BMDMs on day 7 were exposed to GO, and cell morphologies were monitored under a microscope.

For the assessment of GO accumulation inside macrophages, FITC-BSA labeled GO was exposed to cells, and GO outside of cells was washed off with PBS, followed by FACS analysis of the intracellular FITC fluorescence. The labeling of FITC-conjugated BSA on GO was performed as described previously.[73] Labeled GO was washed with PBS for 3 times to remove free FITC-BSA in the supernatant. To evaluate the stability of the FITC-BSA-GO complex, FITC-BSA-GO was spun down 2 days after the initial preparation, and no reduction of florescence was found after resuspension (data not shown), suggesting that the complex was stable at least for 48 h.

Cell Counting, Proliferation Assay, and qRT-PCR Analysis. For cell counting, cells were seeded in 24-well plates with 1.0×10^5 cells/well, and starved in medium with 1% serum for 12 h. Thereafter, cells were treated with GO at 10, 20, 40, and 80 μg/mL. After 24 and 48 h, live cell counting was performed with a hemocytometer after trypan blue staining. BrdU incorporation assay was carried out to evaluate the influence of GO exposure on proliferation of cells following the instructions from the manufacturer (Roche). Total RNAs were extracted from cells using Trizol (Invitrogen), and qRT-PCR analysis was performed as previously described.[43] GAPDH was used as an internal control.

Confocal Laser Scanning Microscopy and Confocal microRaman Spectroscopy. After GO treatment, cells were fixed with 10% PBS-buffered formaldehyde followed by washing with 0.1% Triton X-100 in PBS for 10 min. Cell nuclei were stained with DAPI (blue), and F-actin in cytoskeleton was stained with FITC-conjugated phalloidin (green). Fluorescent images were visualized through confocal laser scanning microscopy as described previously.[43] The fluorescence intensity for F-actin labeled with FITC-conjugated phalloidin was quantified with the software Image J (NIH).

A confocal microRaman spectrometer was employed to characterize GO within cells as described previously.[74,75] In brief, cells were cultured on glass slides and exposed to 40 μg/mL GO for 24 h. Slides were excited with a 532 nm laser after washing 3 times with PBS. Raman mapping was recorded at a $36 \times 36\ \mu m^2$ area with a step size of 3 μm. The images were obtained by collecting the Raman spectrum at each spot (10 s acquisition time, curve from 1200 to 1500 cm^{-1}).

TEM Assessment of GO-Exposed Cells. TEM was used to reveal the distribution of GO within cells. Cells were treated with 40 μg/mL GO for 24 h, and were then washed 3 times with PBS. Cells were collected and fixed in 2.5% glutaraldehyde for 2 h, followed by washing with PBS. Postfixation staining was performed using 1% osmium tetroxide for 1 h at room temperature (RT). After washing, cells were dehydrated using alcohol (40, 50, 70, 80, 90, 95, and 100% ethanol), and treated twice with propylene oxide for 30 min followed by treatment with propylene oxide, Spurr's low viscosity resin (1:1), for 18 h. Cells were further treated with pure resin for 24 h and embedded in beem capsules containing pure resin. Resin blocks were hardened at 70 °C for 2 d. Sections (70 nm) were cut and stained with 1% lead citrate and 0.5% uranyl acetate, and then analyzed under JEOL JEM 2010F.

ROCK Activity Assay. Cells were treated with 10 and 80 μg/mL GO for 24 h. After washing with ice-cold PBS, an equal number of cells was lysed with RIPA lysis buffer (Pierce). ROCK activity was measured with the ROCK activity assay kit (Millipore) according to the manufacturer's instructions. For the acellular ROCK activity assay, purified ROCK in the same kit from Millipore was used. In brief, 10 mUnits (at 1 mUnit/mL) ROCK was incubated along with other required reagents in MYPT1-precoated wells with or without addition of GO followed by the standard procedure provided by the manufacturer.

Cell Death Assay by FACS Analysis and Western Blot analysis. Cells after various treatments were subject to FITC-conjugated Annexin V and PI staining, and apoptotic and necrotic cells were analyzed by FACS as described previously.[43] After washing with PBS, cells were lysed with RIPA lysis buffer, and the same amount of protein extracts was loaded for separation on 12% SDS-PAGE, followed by Western blot analysis as described previously.[43] The antibodies used here were anti-caspase-3 (1:200, Cell Signaling Technology), anti-RIP1 (1:1,500, BD Biosciences), anti-RIP3 (1:1,500, ProSci), or anti-GAPDH (1:1,000, Santa Cruz Biotechnology).

ROS Measurement and ELISA. Cells were cultured in 96-well plates, and preincubated with 10 μM dichlorofluorescein-diacetate (DCF-DA, Sigma) for 30 min. Thereafter, cells were washed with PBS, and treated with GO. The emission spectra of DCF fluorescence at 525 nm using excitation wavelength at 488 nm were monitored on a plate reader or assayed by FACS as previously described.[76,77] The fluorescence intensity was proportional to the intracellular ROS concentration. Mitochondrial superoxide assay was carried out using a specific mitochondrial superoxide indicator, MitoSOX red (Molecular Probes, Invitrogen), according to the manufacturer's instruction. Regarding experiments with NAC, cells were pretreated with 500 μM NAC (Sigma) 1 h prior to GO treatment, and were cultured for another 3 h in the presence of NAC. TNF-α protein production in culture medium of macrophages was measured with a kit from R&D Systems as previously described.[32]

Phagocytosis by Macrophages. Amine-modified red fluorescent latex beads with a mean diameter of 1 μm (Sigma-Aldrich) were opsonized in newborn calf serum for 30 min at 37 °C. After 24 h exposure to GO at 1 and 10 μg/mL, J774.1 cells were incubated with opsonized beads at a final concentration of 0.1% (v/v) for 1 h at 37 °C, and washed twice with PBS followed by FACS analysis to measure the number of cells containing engulfed latex beads and the mean fluorescent intensity in red bead-laden cells.

Statistical Analysis. The difference of experimental data between two groups was assessed using the two-tailed Student's *t* test. One-way analysis of variance (ANOVA) was used to analyze the mean difference among groups compared to the control. Data were shown in mean $\pm$ SD $p < 0.05$ was considered statistically significant.

Conflict of Interest: The authors declare no competing financial interest.

Acknowledgment. This work was supported by grants from the National Natural Science Foundation of China (grant numbers: 21077128, 20921063, 21177151, 21207152), and from the program, "Hundreds Talents", from the Chinese Academy of Sciences. T.X. was supported by US Public Health Service Grant U19 ES019528 (UCLA Center for NanoBiology and Predictive Toxicology). We thank the laboratory members for their great assistance with the experiments and reagents. We thank Lei Sun for technical support with TEM.

Supporting Information Available: Additional results related to this work are provided. This material is available free of charge *via* the Internet at http://pubs.acs.org.

REFERENCES AND NOTES

1. Feng, L. Z.; Liu, Z. A. Graphene in Biomedicine: Opportunities and Challenges. *Nanomedicine* **2011**, *6*, 317–324.
2. Wang, Y. H.; Li, Z. H.; Wang, J.; Li, J. H.; Lin, Y. H. Graphene and Graphene Oxide: Biofunctionalization and Applications in Biotechnology. *Trends Biotechnol.* **2011**, *29*, 205–212.
3. Geim, A. K. Graphene: Status and Prospects. *Science* **2009**, *324*, 1530–1534.
4. Robinson, J. T.; Tabakman, S. M.; Liang, Y. Y.; Wang, H. L.; Casalongue, H. S.; Vinh, D.; Dai, H. J. Ultrasmall Reduced Graphene Oxide with High near-Infrared Absorbance for Photothermal Therapy. *J. Am. Chem. Soc.* **2011**, *133*, 6825–6831.
5. Sun, X. M.; Liu, Z.; Welsher, K.; Robinson, J. T.; Goodwin, A.; Zaric, S.; Dai, H. J. Nano-Graphene Oxide for Cellular Imaging and Drug Delivery. *Nano Res.* **2008**, *1*, 203–212.
6. Liu, Z.; Robinson, J. T.; Sun, X.; Dai, H. Pegylated Nanographene Oxide for Delivery of Water-Insoluble Cancer Drugs. *J. Am. Chem. Soc.* **2008**, *130*, 10876–10877.
7. Yang, K.; Zhang, S.; Zhang, G.; Sun, X.; Lee, S. T.; Liu, Z. Graphene in Mice: Ultrahigh *in Vivo* Tumor Uptake and

Efficient Photothermal Therapy. *Nano Lett.* **2010**, *10*, 3318–3323.
8. Yang, K.; Wan, J. M.; Zhang, S. A.; Zhang, Y. J.; Lee, S. T.; Liu, Z. A. *In Vivo* Pharmacokinetics, Long-Term Biodistribution, and Toxicology of PEGylated Graphene in Mice. *ACS Nano* **2011**, *5*, 516–522.
9. Wang, K.; Ruan, J.; Song, H.; Zhang, J. L.; Wo, Y.; Guo, S. W.; Cui, D. X. Biocompatibility of Graphene Oxide. *Nanoscale Res. Lett.* **2011**, *6*, 8.
10. Zhang, Y. B.; Ali, S. F.; Dervishi, E.; Xu, Y.; Li, Z. R.; Casciano, D.; Biris, A. S. Cytotoxicity Effects of Graphene and Single-Wall Carbon Nanotubes in Neural Phaeochromocytoma-Derived PC12 Cells. *ACS Nano* **2010**, *4*, 3181–3186.
11. Varin, A.; Gordon, S. Alternative Activation of Macrophages: Immune Function and Cellular Biology. *Immunobiology* **2009**, *214*, 630–641.
12. Liao, K. H.; Lin, Y. S.; Macosko, C. W.; Haynes, C. L. Cytotoxicity of Graphene Oxide and Graphene in Human Erythrocytes and Skin Fibroblasts. *ACS Appl. Mater. Interfaces* **2011**, *3*, 2607–2615.
13. Singh, S. K.; Singh, M. K.; Nayak, M. K.; Kumari, S.; Shrivastava, S.; Gracio, J. J. A.; Dash, D. Thrombus Inducing Property of Atomically Thin Graphene Oxide Sheets. *ACS Nano* **2011**, *5*, 4987–4996.
14. Sasidharan, A.; Panchakarla, L. S.; Sadanandan, A. R.; Ashokan, A.; Chandran, P.; Girish, C. M.; Menon, D.; Nair, S. V.; Rao, C. N.; Koyakutty, M. Hemocompatibility and Macrophage Response of Pristine and Functionalized Graphene. *Small* **2012**, *8*, 1251–1263.
15. Sasidharan, A.; Panchakarla, L. S.; Chandran, P.; Menon, D.; Nair, S.; Rao, C. N. R.; Koyakutty, M. Differential Nano-Bio Interactions and Toxicity Effects of Pristine *versus* Functionalized Graphene. *Nanoscale* **2011**, *3*, 2461–2464.
16. Li, Y.; Liu, Y.; Fu, Y. J.; Wei, T. T.; Le Guyader, L.; Gao, G.; Liu, R. S.; Chang, Y. Z.; Chen, C. Y. The Triggering of Apoptosis in Macrophages by Pristine Graphene through the MAPK and TGF-Beta Signaling Pathways. *Biomaterials* **2012**, *33*, 402–411.
17. Chen, G. Y.; Yang, H. J.; Lu, C. H.; Chao, Y. C.; Hwang, S. M.; Chen, C. L.; Lo, K. W.; Sung, L. Y.; Luo, W. Y.; Tuan, H. Y.; *et al.* Simultaneous Induction of Autophagy and Toll-Like Receptor Signaling Pathways by Graphene Oxide. *Biomaterials* **2012**, *33*, 6559–6569.
18. Cho, Y. S.; Challa, S.; Moquin, D.; Genga, R.; Ray, T. D.; Guildford, M.; Chan, F. K. Phosphorylation-Driven Assembly of the RIP1-RIP3 Complex Regulates Programmed Necrosis and Virus-Induced Inflammation. *Cell* **2009**, *137*, 1112–1123.
19. Han, J. H.; Zhong, C. Q.; Zhang, D. W. Programmed Necrosis: Backup to and Competitor with Apoptosis in the Immune System. *Nat. Immunol.* **2011**, *12*, 1143–1149.
20. Fortes, G. B.; Alves, L. S.; de Oliveira, R.; Dutra, F. F.; Rodrigues, D.; Fernandez, P. L.; Souto-Padron, T.; De Rosa, M. J.; Kelliher, M.; Golenbock, D.; *et al.* Heme Induces Programmed Necrosis on Macrophages through Autocrine TNF and ROS Production. *Blood* **2012**, *119*, 2368–2375.
21. Vandenabeele, P.; Galluzzi, L.; Vanden Berghe, T.; Kroemer, G. Molecular Mechanisms of Necroptosis: An Ordered Cellular Explosion. *Nat. Rev. Mol. Cell Biol.* **2010**, *11*, 700–714.
22. Challa, S.; Chan, F. K. M. Going up in Flames: Necrotic Cell Injury and Inflammatory Diseases. *Cell. Mol. Life Sci.* **2010**, *67*, 3241–3253.
23. Poltorak, A.; He, X. L.; Smirnova, I.; Liu, M. Y.; Van Huffel, C.; Du, X.; Birdwell, D.; Alejos, E.; Silva, M.; Galanos, C.; *et al.* Defective LPS Signaling in C3H/HeJ and C57BL/10ScCr Mice: Mutations in TLR4 Gene. *Science* **1998**, *282*, 2085–2088.
24. Verma, A.; Ngundi, M. M.; Meade, B. D.; De Pascalis, R.; Elkins, K. L.; Burns, D. L. Analysis of the Fc Gamma Receptor-Dependent Component of Neutralization Measured by Anthrax Toxin Neutralization Assays. *Clin. Vaccine Immunol.* **2009**, *16*, 1405–1412.
25. Godek, M. L.; Duchsherer, N. L.; McElwee, Q.; Grainger, D. W. Morphology and Growth of Murine Cell Lines on Model Biomaterials. *Biomed. Sci. Instrum.* **2004**, *40*, 7–12.
26. Nicholson, D. W.; Ali, A.; Thornberry, N. A.; Vaillancourt, J. P.; Ding, C. K.; Gallant, M.; Gareau, Y.; Griffin, P. R.; Labelle, M.; Lazebnik, Y. A.; *et al.* Identification and Inhibition of the ICE/CED-3 Protease Necessary for Mammalian Apoptosis. *Nature* **1995**, *376*, 37–43.
27. Bohrer, D.; Horner, R.; do Nascimento, P. C.; Adaime, M.; Pereira, M. E.; Martins, A. F.; Hartz, S. A. Interference in the Limulus Amebocyte Lysate Assay for Endotoxin Determination in Peritoneal Dialysis Fluids and Concentrates for Hemodialysis. *J. Pharm. Biomed. Anal.* **2001**, *26*, 811–818.
28. Huang, K. J.; Niu, D. J.; Sun, J. Y.; Han, C. H.; Wu, Z. W.; Li, Y. L.; Xiong, X. Q. Novel Electrochemical Sensor Based on Functionalized Graphene for Simultaneous Determination of Adenine and Guanine in DNA. *Colloid Surf., B* **2011**, *82*, 543–549.
29. Singh, S. K.; Singh, M. K.; Kulkarni, P. P.; Sonkar, V. K.; Gracio, J. J. A.; Dash, D. Amine-Modified Graphene. Thrombo-Protective Safer Alternative to Graphene Oxide for Biomedical Applications. *ACS Nano* **2012**, *6*, 2731–2740.
30. Zhou, H. J.; Zhao, K.; Li, W.; Yang, N.; Liu, Y.; Chen, C. Y.; Wei, T. T. The Interactions between Pristine Graphene and Macrophages and the Production of Cytokines/Chemokines *via* TLR- and NF-KappaB-Related Signaling Pathways. *Biomaterials* **2012**, *33*, 6933–6942.
31. Li, S. T.; Wang, L. Y.; Berman, M.; Kong, Y. Y.; Dorf, M. E. Mapping a Dynamic Innate Immunity Protein Interaction Network Regulating Type I Interferon Production. *Immunity* **2011**, *35*, 426–440.
32. Wei, Y.; Wang, B.; Wu, J.; Yang, R.; Dunn, M. L. Bending Rigidity and Gaussian Bending Stiffness of Single-Layered Graphene. *Nano Lett.* **2013**, *13*, 26–30.
33. Linkermann, A.; Brasen, J. H.; De Zen, F.; Weinlich, R.; Schwendener, R. A.; Green, D. R.; Kunzendorf, U.; Krautwald, S. Dichotomy between RIP1- and RIP3-Mediated Necroptosis in Tumor Necrosis Factor-Alpha-Induced Shock. *Mol. Med.* **2012**, *18*, 577–586.
34. Cho, Y.; Challa, S.; Moquin, D.; Genga, R.; Ray, T. D.; Guildford, M.; Chan, F. K. M. Phosphorylation-Driven Assembly of the RIP1-RIP3 Complex Regulates Programmed Necrosis and Virus-Induced Inflammation. *Cell* **2009**, *137*, 1112–1123.
35. Festjens, N.; Vanden Berghe, T.; Cornelis, S.; Vandenabeele, P. RIP1, a Kinase on the Crossroads of a Cell's Decision to Live or Die. *Cell Death Differ.* **2007**, *14*, 400–410.
36. Aoki, K.; Saito, H.; Itzstein, C.; Ishiguro, M.; Shibata, T.; Blanque, R.; Mian, A. H.; Takahashi, M.; Suzuki, Y.; Yoshimatsu, M.; *et al.* A TNF Receptor Loop Peptide Mimic Blocks Rank Ligand-Induced Signaling, Bone Resorption, and Bone Loss. *J. Clin. Invest.* **2006**, *116*, 1525–1534.
37. McComb, S.; Cheung, H. H.; Korneluk, R. G.; Wang, S.; Krishnan, L.; Sad, S. cIAP1 and cIAP2 Limit Macrophage Necroptosis by Inhibiting RIP1 and RIP3 Activation. *Cell Death Differ.* **2012**, 1791–1801.
38. Vanlangenakker, N.; Bertrand, M. J. M.; Bogaert, P.; Vandenabeele, P.; Vanden Berghe, T. TNF-Induced Necroptosis in L929 Cells is Tightly Regulated by Multiple TNFR1 Complex I and II Members. *Cell Death Dis.* **2011**, *2*, e230.
39. Tamura, Y.; Chiba, Y.; Tanioka, T.; Shimizu, N.; Shinozaki, S.; Yamada, M.; Kaneki, K.; Mori, S.; Araki, A.; Ito, H.; *et al.* No Donor Induces Nec-1-Inhibitable, but RIP1-Independent, Necrotic Cell Death in Pancreatic Beta-Cells. *FEBS Lett.* **2011**, *585*, 3058–3064.
40. Roychowdhury, S.; McMullen, M. R.; Pisano, S. G.; Liu, X. L.; Nagy, L. E. Absence of Receptor Interacting Protein Kinase 3 Prevents Ethanol-Induced Liver Injury. *Hepatology* **2012**, *57*, 1773–1783.
41. Azijli, K.; Yuvaraj, S.; Peppelenbosch, M. P.; Wurdinger, T.; Dekker, H.; Joore, J.; van Dijk, E.; Quax, W. J.; Peters, G. J.; de Jong, S.; *et al.* Kinome Profiling of Non-Canonical TRAIL Signaling Reveals RIP1-Src-STAT3-Dependent Invasion in Resistant Non-Small Cell Lung Cancer Cells. *J. Cell Sci.* **2012**, *125*, 4651–4661.
42. Degterev, A.; Hitomi, J.; Germscheid, M.; Ch'en, I. L.; Korkina, O.; Teng, X.; Abbott, D.; Cuny, G. D.; Yuan, C.; Wagner, G.; *et al.* Identification of RIP1 Kinase as a Specific Cellular Target of Necrostatins. *Nat. Chem. Biol.* **2008**, *4*, 313–321.
43. Liu, S. J.; Goldstein, R. H.; Scepansky, E. M.; Rosenblatt, M. Inhibition of Rho-Associated Kinase Signaling Prevents

Breast Cancer Metastasis to Human Bone. *Cancer Res.* **2009**, *69*, 8742–8751.
44. Johnson-Lyles, D. N.; Peifley, K.; Lockett, S.; Neun, B. W.; Hansen, M.; Clogston, J.; Stern, S. T.; McNeil, S. E. Fullerenol Cytotoxicity in Kidney Cells Is Associated with Cytoskeleton Disruption, Autophagic Vacuole Accumulation, and Mitochondrial Dysfunction. *Toxicol. Appl. Pharmacol.* **2010**, *248*, 249–258.
45. Liu, S. J.; Suragani, R. N. V. S.; Wang, F. D.; Han, A. P.; Zhao, W. T.; Andrews, N. C.; Chen, J. J. The Function of Heme-Regulated eIF2 Alpha Kinase in Murine Iron Homeostasis and Macrophage Maturation. *J. Clin. Invest.* **2007**, *117*, 3296–3305.
46. Riento, K.; Ridley, A. J. Rocks: Multifunctional Kinases in Cell Behaviour. *Nat. Rev. Mol. Cell Biol.* **2003**, *4*, 446–456.
47. Uehata, M.; Ishizaki, T.; Satoh, H.; Ono, T.; Kawahara, T.; Morishita, T.; Tamakawa, H.; Yamagami, K.; Inui, J.; Maekawa, M.; *et al.* Calcium Sensitization of Smooth Muscle Mediated by a Rho-Associated Protein Kinase in Hypertension. *Nature* **1997**, *389*, 990–994.
48. Liu, S. J. The Rock Signaling and Breast Cancer Metastasis. *Mol. Biol. Rep.* **2011**, *38*, 1363–1366.
49. Matsuzawa, A.; Saegusa, K.; Noguchi, T.; Sadamitsu, C.; Nishitoh, H.; Nagai, S.; Koyasu, S.; Matsumoto, K.; Takeda, K.; Ichijo, H. ROS-Dependent Activation of the TRAF6-ASK1-p38 Pathway Is Selectively Required for TLR4-Mediated Innate Immunity. *Nat. Immunol.* **2005**, *6*, 587–592.
50. Nel, A.; Xia, T.; Madler, L.; Li, N. Toxic Potential of Materials at the Nanolevel. *Science* **2006**, *311*, 622–627.
51. Sayes, C. M.; Gobin, A. M.; Ausman, K. D.; Mendez, J.; West, J. L.; Colvin, V. L. Nano-C60 Cytotoxicity Is Due to Lipid Peroxidation. *Biomaterials* **2005**, *26*, 7587–7595.
52. Xia, T.; Kovochich, M.; Brant, J.; Hotze, M.; Sempf, J.; Oberley, T.; Sioutas, C.; Yeh, J. I.; Wiesner, M. R.; Nel, A. E. Comparison of the Abilities of Ambient and Manufactured Nanoparticles to Induce Cellular Toxicity According to an Oxidative Stress Paradigm. *Nano Lett.* **2006**, *6*, 1794–1807.
53. Xia, T. A.; Zhao, Y.; Sager, T.; George, S.; Pokhrel, S.; Li, N.; Schoenfeld, D.; Meng, H. A.; Lin, S. J.; Wang, X.; *et al.* Decreased Dissolution of ZnO by Iron Doping Yields Nanoparticles with Reduced Toxicity in the Rodent Lung and Zebrafish Embryos. *ACS Nano* **2011**, *5*, 1223–1235.
54. Jayalakshmi, K.; Sairam, M.; Singh, S. B.; Sharma, S. K.; Ilavazhagan, G.; Banerjee, P. K. Neuroprotective Effect of N-Acetyl Cysteine on Hypoxia-Induced Oxidative Stress in Primary Hippocampal Culture. *Brain Res.* **2005**, *1046*, 97–104.
55. Chen, L. Q.; Qu, G. B.; Sun, X.; Zhang, S. P.; Wang, L.; Sang, N. G.; Du, Y. G.; Liu, J.; Liu, S. J. Characterization of the Interaction between Cadmium and Chlorpyrifos with Integrative Techniques in Incurring Synergistic Hepatoxicity. *PLoS One* **2013**, *8*, e59553.
56. Colvin, V. L. The Potential Environmental Impact of Engineered Nanomaterials. *Nat. Biotechnol.* **2003**, *21*, 1166–1170.
57. Li, X.; Peng, Y.; Ren, J.; Qu, X. Carboxyl-Modified Single-Walled Carbon Nanotubes Selectively Induce Human Telomeric I-Motif Formation. *Proc. Nat. Acad. Sci. U.S.A.* **2006**, *103*, 19658–19663.
58. Rodriguez-Fernandez, L.; Valiente, R.; Gonzalez, J.; Villegas, J. C.; Fanarraga, M. L. Multiwalled Carbon Nanotubes Display Microtubule Biomimetic Properties *in Vivo*, Enhancing Microtubule Assembly and Stabilization. *ACS Nano* **2012**, *6*, 6614–6625.
59. Zhu, Y. W.; Murali, S.; Cai, W. W.; Li, X. S.; Suk, J. W.; Potts, J. R.; Ruoff, R. S. Graphene and Graphene Oxide: Synthesis, Properties, and Applications. *Adv. Mater.* **2010**, *22*, 3906–3924.
60. Nguyen, P.; Berry, V. Graphene Interfaced with Biological Cells: Opportunities and Challenges. *J. Phys. Chem. Lett.* **2012**, *3*, 1024–1029.
61. Nel, A. E.; Madler, L.; Velegol, D.; Xia, T.; Hoek, E. M. V.; Somasundaran, P.; Klaessig, F.; Castranova, V.; Thompson, M. Understanding Biophysicochemical Interactions at the Nano-Bio Interface. *Nat. Mater.* **2009**, *8*, 543–557.
62. Mu, Q.; Du, G.; Chen, T.; Zhang, B.; Yan, B. Suppression of Human Bone Morphogenetic Protein Signaling by Carboxylated Single-Walled Carbon Nanotubes. *ACS Nano* **2009**, *3*, 1139–1144.
63. Zhang, H. Y.; Xia, T.; Meng, H.; Xue, M.; George, S.; Ji, Z. X.; Wang, X.; Liu, R.; Wang, M. Y.; France, B.; *et al.* Differential Expression of Syndecan-1 Mediates Cationic Nanoparticle Toxicity in Undifferentiated *versus* Differentiated Normal Human Bronchial Epithelial Cells. *ACS Nano* **2011**, *5*, 2756–2769.
64. Jia, X. T.; Hofmann, M.; Meunier, V.; Sumpter, B. G.; Campos-Delgado, J.; Romo-Herrera, J. M.; Son, H. B.; Hsieh, Y. P.; Reina, A.; Kong, J.; *et al.* Controlled Formation of Sharp Zigzag and Armchair Edges in Graphitic Nanoribbons. *Science* **2009**, *323*, 1701–1705.
65. Qu, G. B.; Wang, X. Y.; Wang, Z.; Liu, S. J.; Jiang, G. B. Cytotoxicity of Quantum Dots and Graphene Oxide to Erythroid Cells and Macrophages. *Nanoscale Res. Lett.* **2013**, *8*, 198.
66. Jorda, E. G.; Verdaguer, E.; Jimenez, A.; de Arriba, S. G.; Allgaier, C.; Pallas, M.; Camins, A. Evaluation of the Neuronal Apoptotic Pathways Involved in Cytoskeletal Disruption-Induced Apoptosis. *Biochem. Pharmacol.* **2005**, *70*, 470–480.
67. Sandbo, N.; Dulin, N. Featured New Investigator Actin Cytoskeleton in Myofibroblast Differentiation: Ultrastructure Defining Form and Driving Function. *Transl. Res.* **2011**, *158*, 181–196.
68. Kristensen, B. W.; Noer, H.; Gramsbergen, J. B.; Zimmer, J.; Noraberg, J. Colchicine Induces Apoptosis in Organotypic Hippocampal Slice Cultures. *Brain Res.* **2003**, *964*, 264–278.
69. Schindler, B.; Segal, E. *Candida albicans* Metabolite Affects the Cytoskeleton and Phagocytic Activity of Murine Macrophages. *Med. Mycol.* **2008**, *46*, 251–258.
70. Fettucciari, K.; Quotadamo, F.; Noce, R.; Palumbo, C.; Modesti, A.; Rosati, E.; Mannucci, R.; Bartoli, A.; Marconi, P. Group B Streptococcus (Gbs) Disrupts by Calpain Activation the Actin and Microtubule Cytoskeleton of Macrophages. *Cell. Microbiol.* **2011**, *13*, 859–884.
71. Liu, Q.; Shi, J. B.; Sun, J. T.; Wang, T.; Zeng, L. X.; Jiang, G. B. Graphene and Graphene Oxide Sheets Supported on Silica as Versatile and High-Performance Adsorbents for Solid-Phase Extraction. *Angew. Chem., Int. Ed.* **2011**, *50*, 5913–5917.
72. Zhou, H. Y.; Mu, Q. X.; Gao, N. N.; Liu, A. F.; Xing, Y. H.; Gao, S. L.; Zhang, Q.; Qu, G. B.; Chen, Y. Y.; Liu, G.; *et al.* A Nano-Combinatorial Library Strategy for the Discovery of Nanotubes with Reduced Protein-Binding, Cytotoxicity, and Immune Response. *Nano Lett.* **2008**, *8*, 859–865.
73. Mu, Q. X.; Su, G. M.; Li, L. W.; Gilbertson, B. O.; Yu, L. H.; Zhang, Q.; Sun, Y. P.; Yan, B. Size-Dependent Cell Uptake of Protein-Coated Graphene Oxide Nanosheets. *ACS Appl. Mater. Interfaces* **2012**, *4*, 2259–2266.
74. Kudin, K. N.; Ozbas, B.; Schniepp, H. C.; Prud'homme, R. K.; Aksay, I. A.; Car, R. Raman Spectra of Graphite Oxide and Functionalized Graphene Sheets. *Nano Lett.* **2008**, *8*, 36–41.
75. Liu, R.; Liu, J. F.; Zhou, X. X.; Sun, M. T.; Jiang, G. B. Fabrication of a Au Nanoporous Film by Self-Organization of Networked Ultrathin Nanowires and Its Application as a Surface-Enhanced Raman Scattering Substrate for Single-Molecule Detection. *Anal. Chem.* **2011**, *83*, 9131–9137.
76. Wang, Z.; Liu, S. J.; Ma, J.; Qu, G. B.; Wang, X. Y.; Yu, S. J.; He, J. Y.; Liu, J. F.; Xia, T.; Jiang, G. B. Silver Nanoparticles Induced RNA Polymerase-Silver Binding and RNA Transcription Inhibition in Erythroid Progenitor Cells. *ACS Nano* **2013**, *28*, 4171–7186.
77. Liu, W.; Zhang, S. P.; Wang, L. X.; Qu, C.; Zhang, C. W.; Hong, L.; Yuan, L.; Huang, Z. H.; Wang, Z.; Liu, S. J.; *et al.* CdSe Quantum Dot (QD)-Induced Morphological and Functional Impairments to Liver in Mice. *PLoS One* **2011**, *6*, e24406.